Supplemental Methods

Tracer Synthesis

^{11}C-PIB was produced from demethyl-PIB and ^{11}C-methyltriflate. High specific activity ^{11}C-CH_3I was prepared in an automated module (PETtrace MeI Microlab, GE Healthcare) and was transformed online to ^{11}C-methyltriflate. The radiolabeling was performed using 1 mg of precursor in acetone in a specialized PET tracer synthesizer for ^{11}C-methylations (GE Healthcare). After purification and formulation, the sterile-filtered product was obtained at 58±2% radiochemical yield with respect to ^{11}C-methyltriflate.

The specific activity was calculated to be 80–120 GBq/μmol at the end of synthesis. Chemical and radiochemical purities of the formulated radiotracer were >95% as determined by high pressure liquid chromatography.

In Vivo PET Measurements

For ^{11}C-PIB-scans, the mice were placed head-to-head in the center of the field of view of the PET scanner on specialized mouse brain beds (Medres) with stereotactic holders. The body temperature of the animals was maintained at 37±0.1 C throughout the study time using a rectal temperature probe with a feedback controlled warming unit.

^{11}C-PIB-PET scans were reconstructed with Filtered Back Projection, an image zoom of 2 and a 256x256 matrix. These parameters yielded a final in-plane resolution of 0.2x0.2 mm² and a transaxial slice thickness of 0.8 mm. All PET measurements were followed by an 803 s attenuation scan with a rotating ^{57}Co source to correct for photon attenuation (9 different bed positions covered the complete field of view). Further, all PET scans were corrected for ^{11}C decay and dead time and normalization was applied. Finally, the [^{11}C]PIB-PET list mode data were histogrammed in 23 frames (8×30s, 6×60s, 7×300s, 2×450s).

Quantitative In Vivo MR Imaging rCBF Measurements

ASL-MR imaging data were analyzed using a simplified version of the Bloch equation and Matlab R2009a with an in house programmed routine:

$$rCBF = \frac{\lambda}{2TI}\frac{\Delta M\left(TI\right)}{M_0}exp\left(\frac{TI}{T_1}\right)$$

with rCBF: regional cerebral blood flow, λ: blood tissue partition coefficient with λ = 0.9 mL/g (in agreement with the literature (*1*)), ΔM(TI): difference in magnetization at given TI, T_1: mean longitudinal relaxation time of blood and tissue in the C57BL/6 mouse brain with T_1 = 2 s, M_0: tissue equilibrium magnetization and TI: inversion time. T_1 was fixed to 2 s throughout the entire study (*2*), TI was chosen as 1800 ms as described previously (*3, 4*).

MR Imaging Sequence and Measurement Details

7 T MR imaging-tse3DT$_2$: turbo spin echo (tse); TR: 3000 ms; TE: 188 ms; flip angle (fa): 90°; matrix size: 112x112x256; field of view: 24x24x57 mm; acquired and reconstructed isotropic resolution (res): 220 µm; turbo factor (tf): 113; averages (avg): 1; acquisition time (TA): 5:38 min.

7 T MR imaging-single slice pASL: TR: 4.1 s; $TE_{1,2}$: 2.05 ms; fa: 70°; inversion pulse: FOCI; inversion time, TI: 1800 ms; scan time: 7000 ms avg: 1; 30 measurements; in-plane res: 0.39x0.39 µm²; slice thickness: 1.2 mm; TA: 7:28 min.

16.4 T microscopic MR imaging-highres-3DT$_2$*: FLASH3D; TR: 80 ms; TE: 20 ms; fa: 18°; field of view: 21.3 x 10.8 x 8.3 mm³; 30 µm isotropic res; avg: 2. During the imaging procedure, brains were immersed in a perfluoropolyether solution medium (Fomblin®, Ausimont) and positioned in a custom made mouse brain holder.

PET Data Evaluation

For the determination of k2' values, which are essential for the Logan graphical analysis, we employed the simplified reference tissue model (SRTM, (*5*)). For the determination of non-displaceable binding potentials (BP_{ND}), we used the frontal cortex (FC), the temporoparietal cortex (TPC), the hippocampus (Hi) and the thalamus (Th) as target regions and the cerebellum (Ce) as reference region.

For the definition of regions of interest, the summed (30-60 min) ^{11}C-PIB images were superimposed on the individual tse3DT$_2$ images; on the basis of the MR imaging, regions of interest were placed in the FC, TPC, Hi, Th and the Ce. Subsequently, the dedicated PET and MR imaging co-registration was confirmed by an additional examination of the superimposition of the first 480 s of ^{11}C-PIB-PET scans. The rigid image fusion tool of PMOD3.2 was used for all co-registration

processes. Finally, the obtained co-registration matrix was applied to the raw ^{11}C-PIB-PET data.

Data Evaluation of the Voxel-Based Correlation of ^{11}C-PIB-PET and ASL-MR Imaging at 7 T

Gaussian blurring of the ASL-MR imaging scans to the spatial resolution of the ^{11}C-PIB-PET allowed us to implement a voxel-based correlation of both modalities in our data evaluation. First, we compared the data distribution of rCBF- and ^{11}C-PIB-values obtained from ASL-MR imaging and ^{11}C-PIB-PET of both transgenic and littermate control APP23 mice by applying a Gaussian fitting routine to the data distribution with merged datasets of all regions of interest and animals (Main manuscript Fig. 4A,C, Supplemental Fig. 5). For the subsequent, voxel-based analysis of both ^{11}C-PIB-PET and ASL-MR imaging acquisitions at 7 T, the summed (30-60 min) ^{11}C-PIB images, that were coregistered to the individual tse3DT_2 scans, and the two ASL-slices, that were also coregistered to the same tse3DT_2 were used.

After image blurring, the individual voxel-values for all transgenic and littermate control animals, and from all regions of interest for both ^{11}C-PIB-PET (in %ID/cc) and ASL-MR imaging (in mL/min/100 g), were extracted and merged for transgenic and control mice, respectively. The single-voxel data for ^{11}C-PIB and rCBF were extracted from the same regions of interest and subsequently ordered into subsets with a range of 0.05 %ID/cc for ^{11}C-PIB-scans (total data range: 0-2.00 %ID/cc) and 10 mL/min/100g for ASL-scans (total data range: 0-500 mL/min/100g), respectively (Supplemental Fig. 5). This yielded a distribution and absolute voxel-number information for each subset, which was afterwards normalized to the total number of extracted voxels from all animals per group (transgenic and control animals, respectively) and expressed as percent of all group-voxels.

This yielded four normally distributed datasets (transgenic and control mice, with ^{11}C-PIB-PET and ASL-MR imaging, respectively). Then, the following Gaussian fitting routine was applied to all four datasets, to retrieve the mean±2σ data range of the respective Gaussians:

$$y = y_0 + \frac{A}{\sigma\sqrt{\frac{\pi}{2}}} e^{-2\frac{(x-\overline{x})^2}{\sigma^2}}$$

With y: frequency of measured values; y_0: y-intercept; A: amplitude; σ: standard deviation; $\overline{x}$: mean. This allowed the calculation of the mean±2σ data interval comprising 95.45% of all single-voxel values and of the mean+2σ and mean-2σ thresholds (drawn from the control mouse data) that were subsequently used for the two-dimensional voxel-value distribution analysis of all mice.

Amyloid Histology

Mice were euthanized with CO_2 and cervically dislocated. Brains were removed and immediately sent to Australia in 4.5% paraformaldehyde for postmortem microscopic MR imaging.

Subsequently, the brains were washed in phosphate buffered saline (PBS) and immersed in a perfluoropolyether solution medium (Fomblin®, Ausimont) prior to microscopic MR imaging assessments at 16.4 T. After microscopic MR imaging, the brains were retransferred from Australia to Germany, dehydrated, embedded in paraffin and cut into 4 μm thick sections employing a microtome (RM2235, Leica). After rehydration, paraffin sections were quenched for endogenous peroxidases with 0.3% H_2O_2 (30% H_2O_2, Sigma Aldrich) for 30 min, followed by blocking of nonspecific binding with normal goat serum (0.3% Triton X-100, 5% goat serum, 94.7% PBS; Triton X-100: Sigma Aldrich; goat serum: vectastain goat normal serum, Vector Laboratories, Inc.). Subsequently, brain slides were incubated with a primary, polyclonal antibody against full-length Aβ at 4 °C overnight at a dilution of 1:1000 (CN3, polyclonal rabbit-anti-human Aβ, (*6, 7*)). After washing the slides with PBS, the secondary antibody (biotinylated polyclonal goat-anti-rabbit IgG, supplied with goat normal serum, Vector Laboratories) was administered at a dilution of 1:400, again followed by a washing step with PBS and by biotin labeling and by incubation with horseradish peroxidase conjugated to streptavidin. Finally, the slides were incubated with the peroxidase substrate SG Blue supplied with 1.5% H_2O_2 (Vector Laboratories), washed, dehydrated and cover-slipped with Eukitt® embedding medium (Sigma-Aldrich).

Slides were scanned with a Nanozoomer slide reader at a 40x magnification (Hamamatsu). After digitization, the images were converted to monochrome with the PMOD3.2 Image view tool and examined with regions of interest in the FC, TPC, Hi and Th with multi-isocontour detection. The used regions of interest corresponded to the regions of interest used for data evaluation of dedicated in vivo PET and MR

imaging and ex vivo microscopic MR imaging. The area of the tissue of interest occupied with amyloid was estimated from the summed area of the multi-isocontour regions and expressed as percent of the original region of interest.

Supplemental Results

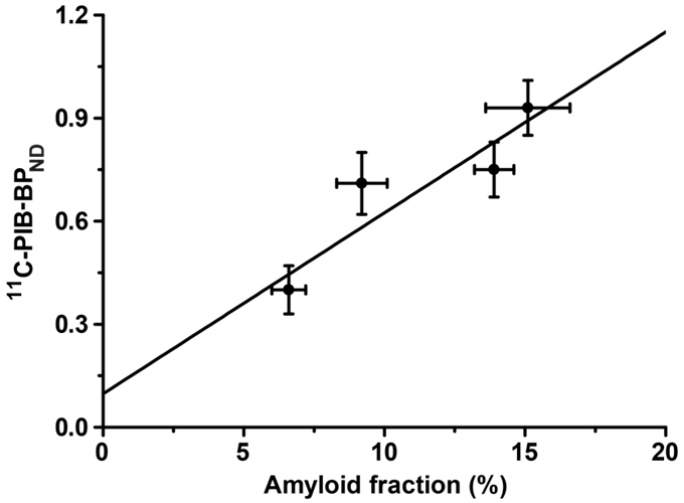

Supplemental FIGURE 1: Correlation of ^{11}C-PIB-BP$_{ND}$ and the histologically assessed amyloid fraction. We observed a positive linear correlation between amyloid ^{11}C-PIB-BP$_{ND}$ and the amyloid positive fraction assessed by amyloid immunohistochemistry ($y = 0.05x + 0.14$, n=5 mice, $R^2 = 0.82$; shown are the mean±SEM of the ^{11}C-PIB-BP$_{ND}$ and amyloid positive fractions of the Th, Hi, TPC and FC, respectively).

Contrast-to-Noise-Ratio of highres-3DT$_2$* Microscopic MR Imaging

Generally, highres-3DT$_2$* microscopic MR imaging allowed the detection of amyloid plaques at a spatial resolution fine enough to examine structural details of single senile plaques (microscopic MR imaging-resolution: 30 µm, amyloid plaque diameter: 25-200 µm, Fig. 3A,B,D, Supplementary Fig. 2) with a contrast-to-noise-ratio of 3.97±0.81. The contrast-to-noise-ratio of amyloid plaques was calculated from (*8*):

$$contrast - to - noise - ratio = \frac{S_t - S_p}{\sqrt{\frac{\sum_{i=1}^{n}\left(S_{pi} - \overline{S_p}\right)^2}{n-1}}}$$

with the numerator: S_t: healthy tissue signal, S_p: amyloid plaque signal; and the denominator: standard deviation of the amyloid plaque signal. Likewise, the contrast-to-noise-ratio of microhemorrhages was calculated as 3.48±0.08.

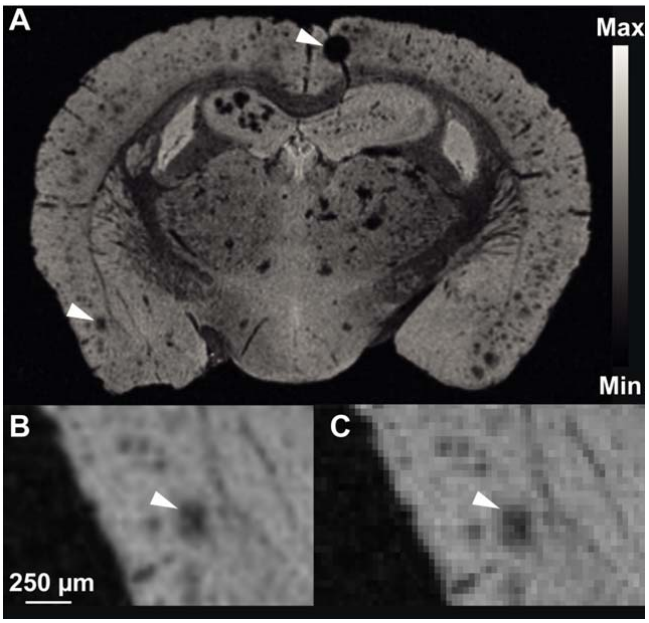

Supplemental FIGURE 2: Highres-3DT$_2$* microscopic MR imaging at single amyloid plaque resolution. (**A**) Example of highres-3DT$_2$* microscopic MR imaging in a 30-month-old transgenic APP23 mouse at the level of the TPC and Hi. Upper middle arrowhead: typical susceptibility artefact induced by a microhemorrhage in the TPC. Lower left arrowhead: large parenchymal amyloid deposit, shown in higher magnification in (**B**) and (**C**) with and without B-spline interpolation, respectively (note the lower T2* grey-values of microhemorrhages in (**A**). In the higher magnification images (**B**,**C**), it is clearly shown that the spatial resolution of the used highres-3DT$_2$* microscopic MR imaging is much higher than the size of the amyloid plaque.

Anatomical Details of Highres-3DT$_2$* Microscopic MR Imaging

Fig. 3C in the main manuscript and Supplemental Fig. 3A show the well-organized structure of the Hi in the healthy mouse brain at high soft-tissue contrast. A higher magnification of both diseased and healthy hippocampi (Supplemental Fig. 3A,C,E) identifies a loss of organization in the transgenic APP23 mouse Hi. The pyramidal cell layer (*Py*), the lacunosum moleculare layer of the hippocampus (*LMol*) and the molecular layer of the dentate gyrus (*Mol*) separating the hippocampal CA1-field and the DG are thinned – in accordance with previous findings (*9, 10*). At the same time, the cytological architecture of the entire Hi is heavily altered – evidenced by highres-3DT$_2$* microscopic MR imaging and confirmed by H&E staining of the corresponding histological sections (Supplemental Fig. 3 A-F).

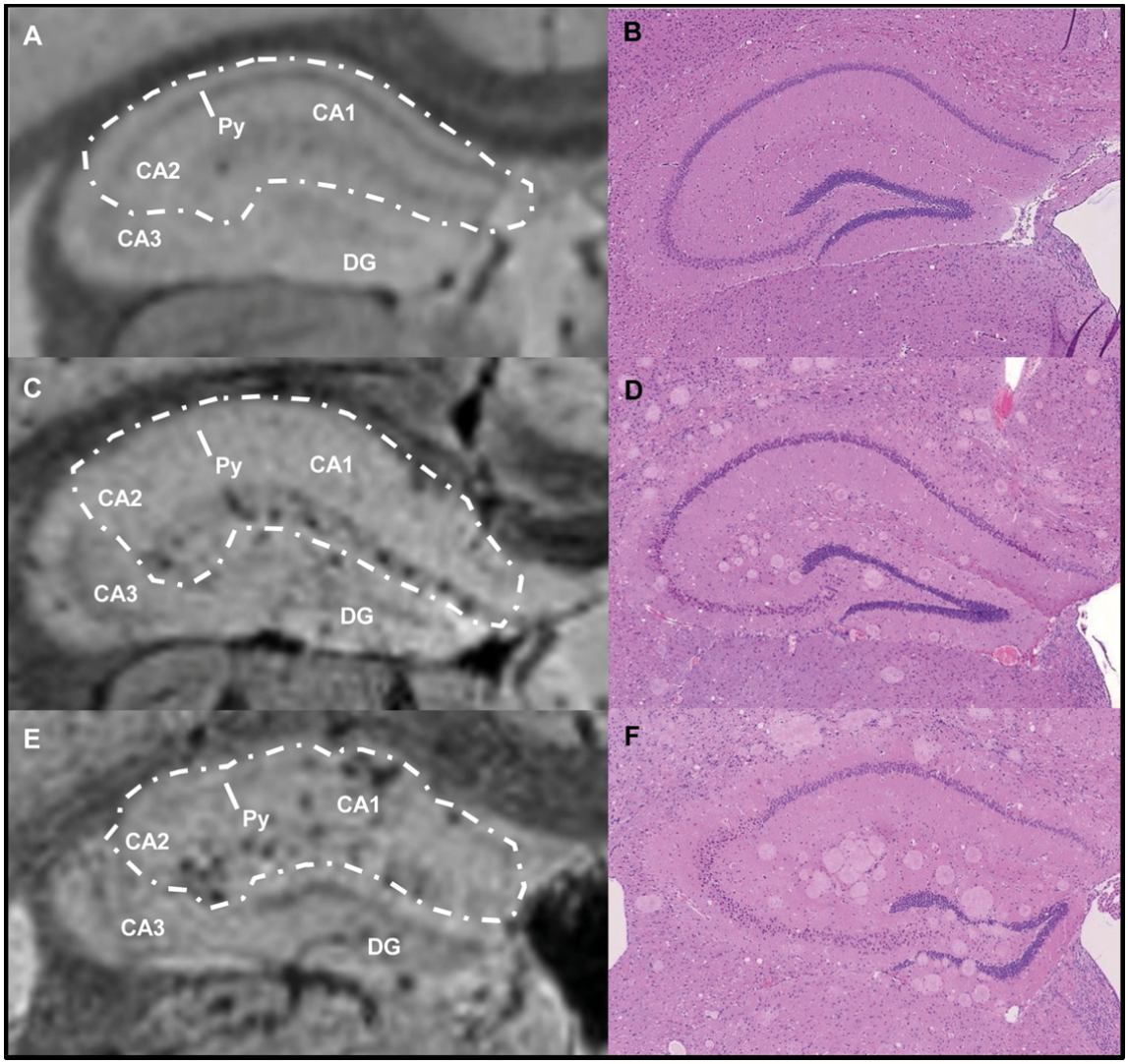

Supplemental FIGURE 3: Highres-3DT_2* microscopic MR imaging of the left Hi in a 27.5-month-old littermate control (A,B), a 27.5-month-old transgenic APP23 (C,D) and in a 30-month-old transgenic APP23 mouse (E,F). (**A,B**) Well organized structure of the Hi in the healthy mouse brain at high soft-tissue contrast; microscopic MR imaging allowed the clear separation of the CA1, CA2, CA3 and DG subfields along with the pyramidal cell layer (*Py*), the lacunosum molecular layer of the hippocampus (*LMol*) and the molecular layer of the dentate gyrus (*Mol*). (**C,D**) Loss of organization of the hippocampus and amyloid plaque deposition in a 27.5-month-old transgenic APP23 mouse. The *Py* can no longer be depicted via microscopic MR imaging; the *LMol* and *Mol* are disorganized. (**E,F**) Severe disruption of the hippocampal architecture in a 30-month-old APP23 mouse. Additionally to the *Py*, both the *LMol* and *Mol* are no longer detectable via microscopic MR imaging.

Voxel-Based Correlation of ^{11}C-PIB-PET and ASL-MR Imaging at 7 T

In general, the Gaussian distribution of rCBF-values in all regions narrowed – meaning that the full width at half maximum (FWHM) of the Gaussians in transgenic mice was significantly lower than the FWHM of the Gaussians in control animals ($FWHM_{tg}$: 84.1±10.3 mL/min/100g, $FWHM_{co}$: 118.9±13.6 mL/min/100g, n=5, $p<0.05$, *t*-test, one-sided, unpaired). The amplitudes (*A*) of the Gaussians in transgenic mice were higher in comparison to littermate control animals (A_{tg}: 11.3±1.4, A_{co}: 8.1±0.8, n=5, $p<0.05$, *t*-test, one-sided, unpaired). Thus, there was a shift to lower rCBF values, the probability for lower rCBF values increased and the Gaussian distribution was narrowing in transgenic APP23 mice (main manuscript Fig. 4B). For ^{11}C-PIB-PET data, a diametrically opposed frequency distribution was found (main manuscript Fig. 4A).

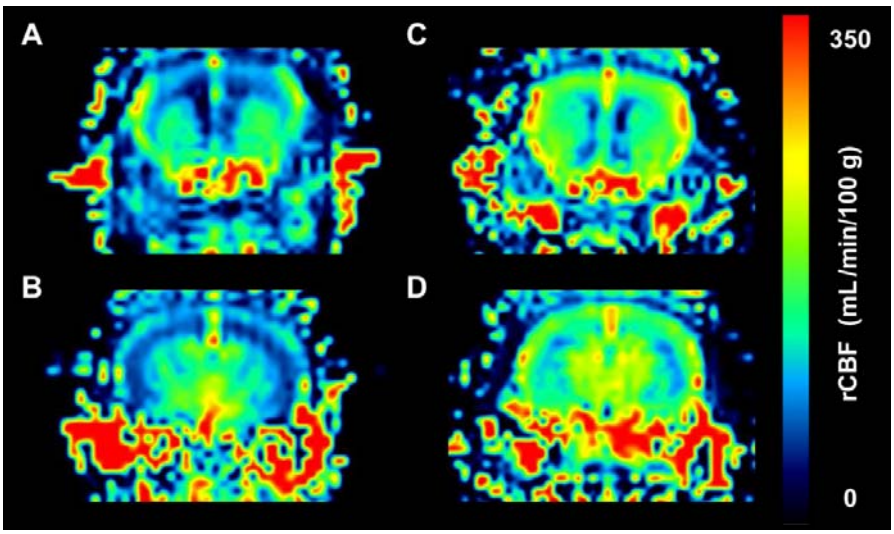

Supplemental FIGURE 4: Representative rCBF maps calculated from ASL-MR imaging in a transgenic and a littermate control APP23 mouse. (**A**,**B**) Quantitative rCBF maps of a 30-month-old transgenic APP23 mouse taken from (**A**) bregma: 0.14 mm, (**B**) bregma: -1.94 mm. Severe reduction of the rCBF was clearly visible in the FC and the TPC, lower loss of rCBF was observed both in the Hi and in the Th. (**C**,**D**) Quantitative rCBF maps of a 30-month-old littermate control APP23 mouse taken from (**A**) bregma: 0.14 mm, (**B**) bregma: -1.94 mm. The regular rCBF pattern observed previously in other mice remained unaltered, despite the high age of the animal. These findings correspond well to our previously published results (*4*).

	mean	mean-2σ	mean+2σ
PIB(co)	**0.29**	**0.08**	**0.50**
ASL(co)	**227**	**124**	**330**
PIB(tg)	*0.85*	*0.42*	*1.28*
ASL(tg)	*147*	*74*	*220*

Supplemental TABLE 1: Cutoff-values for gating of ^{11}C-PIB-PET and ASL-MR imaging voxelwise correlation analysis. Gates were calculated from a 95.45% probability threshold (2σ) derived from the respective Gaussian distributions of littermate control mice; shown are, however, also the 95.45% probability thresholds for transgenic APP23 mice.

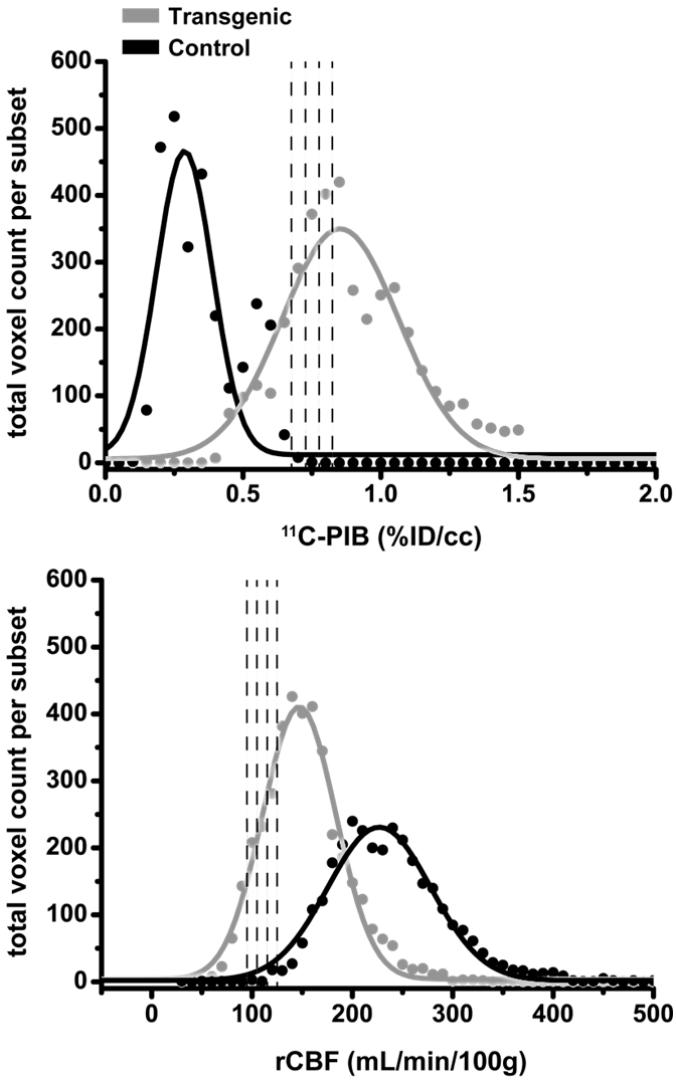

Supplemental FIGURE 5: Total voxel count and voxel distribution per data-subset taken from ^{11}C-PIB-PET and ASL-MR imaging scans from all regions and all pooled animals. Frequency distribution and respective Gaussian fits of ^{11}C-PIB (upper graph) and of rCBF values (lower graph) (black: control mouse data, grey: transgenic animal data). The data were normalized to the total voxel count from each animal group (transgenic n=3903 voxels, control n=3901 voxels, taken from 4 regions and 5 animals per group; plotted in FIGURE 4 in the main manuscript). Examples of data subsets are indicated by dashed lines.

Supplemental Discussion

Advantages of Microscopic MR Imaging over Tissue Clearing Methods and Classical Histological Staining

One major advantage of our used microscopic MR imaging protocol is the intrinsic contrast that does not require further processing or staining with antibodies or contrast agents. The proposed microscopic MR imaging protocol is not dependent upon the external administration of contrast agents, as e.g. in the case of PET-measurements, where the usage of radioactive contrast agents is a prerequisite for every measurement. Another advantage of our microscopic MR imaging approach is the yield of relatively small and easy-to-handle datasets. Chung et al. comment on this point that *"Turning immense datasets into useful insights remains a key challenge"* (*11*). We demonstrate three-dimensional whole-brain imaging of the entire intact mouse brain at 30 μm^3 resolution, yielding datasets of only 120±5 Mbyte (much less data in comparison to a three-dimensional reconstruction from histological data of an entire mouse brain; this easily yields datasets in the Gigabyte range) in DICOM format that can be processed with many different software types that are widely available. Moreover, in comparison to a reconstructed, entirely immunostained brain, the workload is dramatically reduced, as such stainings would require easily two weeks' work, before the reconstruction can be started, whereas our microscopic MR imaging approach has an acquisition time of only 30 min.

Without doubt, the tissue clearing and imaging protocols suggested by Renier et al. (iDISCO (*12*)) and Chung et al. (CLARITY (*11*)), among others (i.e. Hama et al. (*13*) and Susaki et al. (*14*)), are superior in sensitivity and resolution to our microscopic MR imaging approach; however, it will never be possible to transfer any tissue clearing method to an *in vivo* application (for example in rodents), whereas this is well conceivable and intended for our microscopic MR imaging protocol that we suggest in this publication. Moreover, our microscopic MR imaging approach is not only transferable to the in vivo application in mice but also to human patients with the advent of ultra-high field MRI scanners in clinical research (*15, 16*). It can be expected that a field-strength of 11.7 T (currently envisaged in the INUMAC project in Saclay, France; INUMAC will be the world´s first 11.7 T human MRI system for clinical research applications and will be available in 2015 (*17*)) presumably yields a spatial resolution of 200 μm^3 in the living human patient's brain, which should be

sufficient to image amyloid plaque clusters – it might even be possible to image single amyloid plaques if the SNR is sufficiently high. Moreover, the scaling of anatomical structures in the mouse and the human brain needs to be addressed here. Anatomical structures observed by us at a field-strength of 16.4 T at a spatial resolution of 30 μm will be scaled in the human brain and will thus not require the same absolute imaging spatial resolution and field-strength. It is well conceivable that similar structures (along the spatial scale from mouse to man) will be visible in the human patient's brain at lower field-strengths.

Apart from the field of AD imaging research, there are numerous examples of clinically important anatomical features becoming visible at 7 T, e.g. central veins in MS lesions, higher definition of joints, cartilage and cartilage destruction, etc. Equally important are the enhanced contrast mechanisms at higher field-strengths – T_2*, susceptibility weighted imaging, diffusion, CEST, etc. which allow better characterization of tissue and are being applied clinically in various imaging fields. Moreover, the ability to characterize tissue structures at high spatial resolution with microscopic MR imaging is gaining importance in informing the interpretation of human scale imaging. Microscopic MR imaging allows structural and functional analysis of the tissue of interest at an order of magnitude higher resolution than standard clinical systems and so if one understands the constituent contributions that are averaged out in human imaging voxels we can better understand the origin of changes in voxel intensity and contrast. A nice example of this is in prostate imaging performed by one of our collaboration partners in Australia (unpublished data). DWI of normal prostate tissue sections acquired at 16.4 T showed three distinct compartments with different diffusivity corresponding to the fluid in tubules, interstitial tissue and epithelial cell layers. In vivo, resolution is not sufficient to distinguish these compartments so the measured diffusion is the weighted average of the three contributions. In prostate cancer these structures are lost and the tissue is more homogeneous. So, knowledge of the underlying structure and diffusion properties of normal tissue obtained from correlative microscopic MR imaging will potentially allow conclusions about the health of tissue to be drawn from DWI in vivo. So, imaging at high field in animal models is going to be even more relevant for translational imaging studies at high or ultra-high fields.

Duyn et al. report that there are currently more than thirty 7 T human MR imaging systems available worldwide, while 9.4 T systems are already used in clinical

research in Chicago, Minnesota, Juelich and Tuebingen. Systems with fields above 9.4 T are under development in Minnesota, USA (10.5 T), as mentioned in Saclay, France (11.7 T) and lastly in South Korea (14 T) (*15*). Thus, although the costs are immense for such clinical MRI systems with ultra-high field (> 9.4 T), there is an ongoing trend towards pushing the limits of MR imaging physics and towards higher field strengths in human MR imaging scanners. Especially in the field of neurology, this will open new avenues in brain research (*15*).

Limitations of Microscopic MR Imaging

The sole use of microscopic MR imaging to detect amyloid deposits is limited by a lack of specificity, by the combined need of high-CNR-high-resolution sequences, spatial blurring caused by respiratory or pulsative movement (if in vivo microscopic MR imaging is performed) and a number of additional artifacts. These artifacts include the misinterpretation of microscopic MR imaging images by untrained readers, as for example the striated body of the caudate putamen (main manuscript Fig. 2C) could be interpreted as amyloid deposits. However, striatal amyloidosis can be excluded from the corresponding in vivo ^{11}C-PIB-PET in combination with ex vivo amyloid histology. Similarly, as shown in main manuscript Fig. 3C, low T_2* signal intensities are also assigned to blood vessels parallel or orthogonal to the imaging plane (white arrowheads) or to axon bundles like the *mt* or the *PeF* (red arrowheads). As mentioned above, microhemorrhages are another potential source of image misinterpretation, most of which can however be distinguished from senile plaques if the CNR and the intra-deposit CNR pattern is considered (senile plaques are characterized by higher grey-values, main manuscript Fig. 2C, Supplemental Fig. 2). The need for a high CNR is one reason for the use of surface coils; however, in contrast to recently published papers (*18-22*) we employed a volume coil, thus eliminating the usual signal gradient across the scanned object orthogonal to the coil surface. Thus, CNR and amyloid plaques throughout the entire brain were detected in a homogeneous way, enabling a statistical data analysis method as proposed in this paper.

Limitations of Small Animal PET

Partial Volume Effect

Absolute quantification of the acquired PET data is the ultimate goal to achieve in PET. However many factors hamper the quantification accuracy such as attenuation

or scatter correction, as well as the limited spatial resolution, which also varies within the field of view depending on the acquisition position and on the used reconstruction and correction algorithms (*23, 24*). Especially for small animal imaging, the partial volume effect (PVE) is the major cause of quantification degradation, since the structures measured in small animals can be down to 1 mm or smaller typically measured with a spatial resolution of ~1.5 mm resulting in recovery coefficients of down to ~10-20% depending on the contrast ratio, reconstruction and correction algorithm. Whereas in human PET imaging systems, in which the spatial resolution is typically in the range of 5 mm, larger structures are measured and hence degradation of the quantification is less compared to small animal PET scanners. (*25*).

The partial volume effect is coupled to the limited spatial resolution of the distinct PET scanner and consequently to the point spread function (PSF) of each system (*26*). Tremendous effort has been done in the last decades to correct the PVE. Thereby, different approaches have been carried out so far, either based on phantom measurements, which determine the PSF (*26*), or on prior anatomical information acquired with the MRI or CT to gain information about the size of each structure impacted by the PVE (*27*). However, all investigated methods need to be adapted and evaluated for each individual imaging situation to ensure a proper PVE correction of the structures also in terms of dynamic imaging data, where contrast ratios are changing over time due to reversible binding of radioligands.

Positron Range

In addition to the PVE, the spatial resolution of PET is ultimately limited by the positron range – depending on the used isotope (*28, 29*). The mean positron range of ^{11}C was determined by Phelps et al. to 1.1 mm (*28*), while the physical limit regarding the spatial resolution of a typical small animal PET system employing ^{11}C-labeled tracers was computed to ~0.9 mm by Levin and Hoffman using Monte Carlo-based simulations of typical ^{11}C-positron trajectories (*29*). This influences both the image quality and the PVE – and thus, the quantification of small animal amyloid imaging experiments. Novel ^{18}F-labeled amyloid tracers like florbetaben, amyvid (florbetapir) or flutemetamol are promising imaging regimens (already routinely used in daily clinics), as the positron range of ^{18}F is much smaller in tissue in comparison to ^{11}C-positrons, ultimately improving the spatial resolution, the image quality and the signal-to-noise ratio (*29-35*).

Author Contributions

F.C.M., M.D.K., G.J.G., I.M.B. and B.J.P. designed the research. F.C.M. performed the dedicated in vivo PET and MR imaging experiments. M.D.K. performed ex vivo MR imaging experiments. F.C.M. and D.B. performed histology. B.B. read the microscopic MR imaging images. F.C.M. analyzed the data, conducted the statistics and designed the figures. F.C.M. and J.G.M. wrote the manuscript. All authors edited the manuscript.

References

1. Peller M, Kurze V, Loeffler R, et al. Hyperthermia induces T1 relaxation and blood flow changes in tumors. A MRI thermometry study in vivo. *Magn Reson Imaging.* 2003;21:545-551.

2. Zhang X, Petersen ET, Ghariq E, et al. In vivo blood T1 measurements at 1.5 T, 3 T, and 7 T. *Magnetic Resonance in Medicine.* 2012:1082–1086.

3. Kwong KK, Chesler DA, Weisskoff RM, et al. MR perfusion studies with T1-weighted echo planar imaging. *Magn Reson Med.* 1995;34:878-887.

4. Maier FC, Wehrl HF, Schmid AM, et al. Longitudinal PET-MRI reveals [beta]-amyloid deposition and rCBF dynamics and connects vascular amyloidosis to quantitative loss of perfusion. *Nat Med.* 2014;20:1485-1492.

5. Lammertsma AA, Hume SP. Simplified reference tissue model for PET receptor studies. *Neuroimage.* 1996;4:153-158.

6. Eisele YS, Obermuller U, Heilbronner G, et al. Peripherally applied Abeta-containing inoculates induce cerebral beta-amyloidosis. *Science.* 2010;330:980-982.

7. Radde R, Bolmont T, Kaeser SA, et al. Abeta42-driven cerebral amyloidosis in transgenic mice reveals early and robust pathology. *EMBO Rep.* 2006;7:940-946.

8. Chamberlain R, Reyes D, Curran GL, et al. Comparison of amyloid plaque contrast generated by T2-weighted, T2*-weighted, and susceptibility-weighted imaging methods in transgenic mouse models of Alzheimer's disease. *Magn Reson Med.* 2009;61:1158-1164.

9. Mann DM. Pyramidal nerve cell loss in Alzheimer's disease. *Neurodegeneration.* 1996;5:423-427.

10. Calhoun ME, Wiederhold KH, Abramowski D, et al. Neuron loss in APP transgenic mice. *Nature.* 1998;395:755-756.

11. Chung K, Wallace J, Kim SY, et al. Structural and molecular interrogation of intact biological systems. *Nature.* 2013;497:332-337.

12. Renier N, Wu Z, Simon DJ, Yang J, Ariel P, Tessier-Lavigne M. iDISCO: a simple, rapid method to immunolabel large tissue samples for volume imaging. *Cell.* 2014;159:896-910.

13. Hama H, Kurokawa H, Kawano H, et al. Scale: a chemical approach for fluorescence imaging and reconstruction of transparent mouse brain. *Nat Neurosci.* 2011;14:1481-1488.

14. Susaki EA, Tainaka K, Perrin D, et al. Whole-brain imaging with single-cell resolution using chemical cocktails and computational analysis. *Cell.* 2014;157:726-739.

15. Duyn JH. The future of ultra-high field MRI and fMRI for study of the human brain. *Neuroimage.* 2012;62:1241-1248.

16. Kerchner GA. Ultra-high field 7T MRI: a new tool for studying Alzheimer's disease. *J Alzheimers Dis.* 2011;26 Suppl 3:91-95.

17. Vedrine PG, G. ; Aubert, G. ; Belorgey, J. ; Berriaud, C. ; Bourquard, A. ; Bredy, P. ; Donati, A. ; Dubois, O. ; Juster, F.P. ; Lannou, H. ; Molinié, F. ; Nusbaum, M. ; Nunio, F. ; Payn, A. ; Quettier, L. ; Schild, T. ; Scola, L. ; Sinanna, A. ; Stepanov, V. Iseult/INUMAC Whole Body 11.7 T MRI Magnet. *IEEE Transactions on Applied Superconductivity.* 2015.

18. Hartig W, Goldhammer S, Bauer U, et al. Concomitant detection of beta-amyloid peptides with N-terminal truncation and different C-terminal endings in cortical plaques from cases with Alzheimer's disease, senile monkeys and triple transgenic mice. *J Chem Neuroanat.* 2010;40:82-92.

19. Poduslo JF, Wengenack TM, Curran GL, et al. Molecular targeting of Alzheimer's amyloid plaques for contrast-enhanced magnetic resonance imaging. *Neurobiol Dis.* 2002;11:315-329.

20. Wadghiri YZ, Sigurdsson EM, Sadowski M, et al. Detection of Alzheimer's amyloid in transgenic mice using magnetic resonance microimaging. *Magn Reson Med.* 2003;50:293-302.

21. Wengenack TM, Reyes DA, Curran GL, et al. Regional differences in MRI detection of amyloid plaques in AD transgenic mouse brain. *Neuroimage.* 2011;54:113-122.

22. Yang J, Wadghiri YZ, Hoang DM, et al. Detection of amyloid plaques targeted by USPIO-Abeta1-42 in Alzheimer's disease transgenic mice using magnetic resonance microimaging. *Neuroimage.* 2011;55:1600-1609.

23. Visser EP, Disselhorst JA, Brom M, et al. Spatial resolution and sensitivity of the Inveon small-animal PET scanner. *J Nucl Med.* 2009;50:139-147.

24. Erlandsson K, Buvat I, Pretorius PH, Thomas BA, Hutton BF. A review of partial volume correction techniques for emission tomography and their applications in neurology, cardiology and oncology. *Phys Med Biol.* 2012;57:R119-159.

25. Mannheim JG, Wehrl HF, Judenhofer MS, Pichler BJ. Small Animal PET Cameras — Development, Technology, PET/CT, PET/MRI. *Trends on the Role of PET in Drug Development*:289-317.

26. Soret M, Bacharach SL, Buvat I. Partial-volume effect in PET tumor imaging. *J Nucl Med.* 2007;48:932-945.

27. Meltzer CC, Kinahan PE, Greer PJ, et al. Comparative evaluation of MR-based partial-volume correction schemes for PET. *J Nucl Med.* 1999;40:2053-2065.

28. Phelps ME, Hoffman EJ, Huang SC, Ter-Pogossian MM. Effect of positron range on spatial resolution. *J Nucl Med.* 1975;16:649-652.

29. Levin CS, Hoffman EJ. Calculation of positron range and its effect on the fundamental limit of positron emission tomography system spatial resolution. *Phys Med Biol.* 1999;44:781-799.

30. Barthel H, Gertz HJ, Dresel S, et al. Cerebral amyloid-beta PET with florbetaben (18F) in patients with Alzheimer's disease and healthy controls: a multicentre phase 2 diagnostic study. *Lancet Neurol.* 2011;10:424-435.

31. Barthel H, Sabri O. Florbetaben to trace amyloid-beta in the Alzheimer brain by means of PET. *J Alzheimers Dis.* 2011;26 Suppl 3:117-121.

32. FDA approves 18F-florbetapir PET agent. *J Nucl Med.* 2012;53:15N.

33. Clark CM, Pontecorvo MJ, Beach TG, et al. Cerebral PET with florbetapir compared with neuropathology at autopsy for detection of neuritic amyloid-beta plaques: a prospective cohort study. *Lancet Neurol.* 2012;11:669-678.

34. Hatashita S, Yamasaki H, Suzuki Y, Tanaka K, Wakebe D, Hayakawa H. [F]Flutemetamol amyloid-beta PET imaging compared with [C]PIB across the spectrum of Alzheimer's disease. *Eur J Nucl Med Mol Imaging.* 2013.

35. Snellman A, Rokka J, Lopez-Picon FR, et al. Pharmacokinetics of [(1)(8)F]flutemetamol in wild-type rodents and its binding to beta amyloid deposits in a mouse model of Alzheimer's disease. *Eur J Nucl Med Mol Imaging.* 2012;39:1784-1795.